



Sulfur-poisoning on Rh NP but sulfur-promotion on single-Rh₁-site for methanol carbonylation

Siquan Feng^{a,1}, Jiali Mu^{a,1}, Xiangsong Lin^{b,1}, Xiangen Song^{a,*}, Siyue Liu^a, Wen Shi^a, Weiqing Zhang^c, Guorong Wu^c, Yang Jiayue^c, Wenrui Dong^{c,*}, Xueming Yang^{c,d}, Jingwei Li^a, Zheng Jiang^e, Yunjie Ding^{a,f,**}

^a Dalian National Laboratory for Clean Energy, Dalian Institute of Chemical Physics, Chinese Academy of Sciences, 116023 Dalian, China

^b School of Materials and Textile Engineering, Jiaying University, 314001 Jiaxing, China

^c State Key Laboratory of Molecular Reaction Dynamics, Dalian Institute of Chemical Physics, Chinese Academy of Sciences, 116023 Dalian, China

^d Department of Chemistry, Southern University of Science and Technology, 518055 Shenzhen, China

^e Shanghai Synchrotron Radiation Facility, Shanghai Institute of Applied Physics, and Shanghai Advanced Research Institute, Chinese Academy of Sciences, 201204 Shanghai, China

^f State Key Laboratory of Catalysis, Dalian Institute of Chemical Physics, Chinese Academy of Sciences, 116023 Dalian, China

ARTICLE INFO

Keywords:

Sulfur poisoning
Metal nanoparticle catalysts
Sulfur promotion
Single-Rh₁-site catalyst
In situ transformation of H₂S

ABSTRACT

Sulfur poisoning is a severe problem for most noble metal nanoparticle (NP) catalysts, and ppm or ppb levels of sulfur species could result in dramatic activity reduction or even irreversible deactivation. Developing catalysts with high sulfur tolerance is crucial, yet challenging. Here, we reported a clear discovery in methanol carbonylation that sulfur poisoned the Rh NP (Rh/CMK-3) but promoted the single-Rh₁-site (Rh₁/AC) while the Rh NP (Rh/AC) experienced a process of atomic dispersion. Strong adsorption of sulfur and the formation of the Rh-S passivation layer were supposed to lead to Rh/CMK-3 sulfur poisoning. However, the detrimental H₂S transformed into CH₃SCH₃ and CH₃SH on Rh₁/AC and then acted as a ligand of Rh atoms, participating in the subsequent reaction, lowering the energy barrier of the rate-determining step, and lastly promoting the reaction. This work provides benefits in solving the sulfur poisoning of metal NP and developing high sulfur tolerant single-metal-site catalysts.

1. Introduction

Sulfur poisoning is a great challenge for supported metal nanoparticle (NP) catalysts [1–3]. A ppm or ppb level of sulfur in a raw feed could dramatically reduce the activity of metal catalysts, even leading to irreversible deactivation [4,5]. For example, 13 ppb H₂S could lead to severe deactivation for Ni/Al₂O₃ NPs catalysts in methanation reaction during 50 h time on stream [6], and 7 ppm H₂S could lead to 90 % activity loss for Ni-Rh alloy NPs catalysts during methane reforming reaction during 8 h time on stream [7]. The strong adsorption of sulfur species on the surface of metal NPs is deemed to block the active sites and lead to catalyst deactivation [1–7]. The strong adsorption of sulfur species on the surface of metal NP is deemed to block the active sites and

lead to catalyst deactivation [8]. Besides, the formation of metal sulfides and the sulfating of support are also factors of sulfur poisoning for metal NPs catalysts. Great efforts and intensive energy have been paid annually with the desulfurization technique to ensure the long-term activity of metal catalysts in the industry. Therefore, it is significant and urgent to develop an effective strategy promoting the sulfur tolerance of metal catalysts, whether in academia or industry.

Reducing the particle size of metal NPs into sub-nanoscale clusters and even atomic dispersion is promising to provide an opportunity to alleviate the problem mentioned above. Heterogeneous single-metal-site catalysts especially those with single-nuclear are appealing to provide such an opportunity [9–16], given their theoretical 100 % atom efficiency and especially their versatile coordination structure-activity

* Corresponding authors.

** Corresponding author at: Dalian National Laboratory for Clean Energy, Dalian Institute of Chemical Physics, Chinese Academy of Sciences, 116023 Dalian, China.

E-mail addresses: xiangensong@dicp.ac.cn (X. Song), wrdong@dicp.ac.cn (W. Dong), djy@dicp.ac.cn (Y. Ding).

¹ Siquan Feng, Jiali Mu, and Xiangsong Lin contributed equally to this work.

relationship. For example, atomically dispersed Ru_1/NC manifests high resistance against the sulfur poison, and just only 20 % activity loss for 500 ppm thiophene. [10] Liang et al. also reported a sulfur-tethering high-loading atomically dispersed noble metal catalysts (Rh/SC , Ru/SC , Pd/SC , Ir/SC), which demonstrated excellent performance in formic acid oxidation and quinoline hydrogenation [11]. Ding et al. also presented a sulfur-promoted performance in olefin hydrocarboxylation reactions on a single-Rh-site catalyst [17]. Besides, we are interested to found that the ligand with different coordination abilities could co-exist and coordinate with the single-metal-site catalysts, which is different from the metal nanoparticles. The coordination of the inorganic and organic sulfur ligands would possibly result in a reversed sulfur effect and thus solve the sulfur poisoning of H_2S on transition metal catalysts for a single-metal-catalyst. Thus, the in-situ transformation of H_2S into catalyst-friendly organic sulfur ligands, such as CH_3SCH_3 or CH_3SH , is supposed to realize the high sulfur tolerance of single-metal-site catalysts.

Methanol Carbonylation is a kind of reaction concerning the coupling of $\text{C}\equiv\text{O}$ to CH_3I to form the CH_3COI , which would react spontaneously react with the substrate of CH_3OH to form the products of $\text{CH}_3\text{COOCH}_3$ or CH_3COOH [18]. The corresponding catalysts are usually focused on the carbonyl metal complexes of $\text{M}(\text{CO})_x\text{L}_y$ ($\text{M} = \text{Rh}$, Pt , Pd , Ir , and Ru , and L represents varieties of ligands). Our team has conducted in-depth and systematic research on this methanol carbonylation reaction, including single-site Ir_1/AC catalyst [19,20], single-site Rh_1/AC catalyst [21], single-site Rh_1/PIPs catalyst [22,23], single-site dual-core $\text{Ir}_1\text{-La}_1/\text{AC}$ catalyst [24], as well as their concrete reaction mechanism and scientific problems.

Here, a sulfur-poisoning on Rh NP ($\text{Rh}/\text{CMK-3}$) supported on mesoporous carbon but sulfur-promotion on single- Rh_1 -site (Rh_1/AC) supported on activated carbon was thoroughly uncovered for methanol carbonylation reaction with the feedstock stream containing 1000 ppm H_2S , while the Rh NP (Rh/AC) experienced a process of atomic dispersion and the in-situ transformation of noxious H_2S into organic CH_3SCH_3 and CH_3SH components were unambiguously disclosed. The coordination of the sulfur effect of H_2S , CH_3SH , and CH_3SCH_3 on a single- Rh_1 -site (Rh_1/AC) catalyst was explored in detail for the heterogeneous methanol carbonylation reaction.

During the reaction, the Rh NP catalyst ($\text{Rh}/\text{CMK-3}$) was gradually poisoned by H_2S and simultaneously accompanied by the agglomeration of metal atoms, while the single- Rh_1 -site (Rh_1/AC) exhibited even enhanced performance in the presence of 1000 ppm H_2S and the Rh NP catalyst (Rh/AC) experienced an atomic dispersion even under the 1000 ppm H_2S . High-angle annular dark-field scanning transmission electron microscopy (HAADF-STEM), in/ex-situ extended X-ray absorption fine structure (in/ex situ EXAFS) demonstrated that H_2S exhibited neglectable influence on the atomic as well as the electronic structure of Rh_1/AC catalyst, while X-ray photoelectron spectroscopy (XPS), in-situ diffuse reflectance infrared Fourier transform spectroscopy (in-situ DRIFTS), and in-situ free-electron laser time of flight mass spectrometry (in-situ FEL/TOF MS) revealed that the toxic H_2S was quickly transformed into CH_3SCH_3 and CH_3SH species through the reaction with CH_3I and/or CH_3OH . The resulting organic sulfur species (CH_3SCH_3 and CH_3SH) could further promote the carbonylation process as a consequence of being ligands of supported single- Rh_1 -site.

The different sulfur effects of H_2S on Rh NP ($\text{Rh}/\text{CMK-3}$) and single- Rh_1 -site (Rh_1/AC) were highlighted, and the different coordination abilities of organic or inorganic sulfur species with Rh_1/AC were also emphatically addressed. More interestingly, CH_3I and CH_3OH species were the ingredients of methanol carbonylation based on transitional metal Rh , Ir , or Ni catalysts, and high value-added products like methyl acetate or acetate acid with one more carbon were produced after coupling with CO [25,26]. Accordingly, CO and CH_3I were reported as essential elements, leading to the atomic dispersing of noble metal NPs supported on activated carbon (AC) [27]. Therefore, it is foreseeable that H_2S would transform quickly into CH_3SH and CH_3SCH_3 during the

reaction of methanol carbonylation by CH_3I and/or CH_3OH , and the Rh NP (Rh/AC) would experience a process of atomic dispersion to single- Rh_1 -site (Rh_1/AC), accompanied by the increased carbonylation activity in methanol carbonylation by $\text{CO}/\text{CH}_3\text{I}$, whereas it is not on another kind of Rh NPs ($\text{Rh}/\text{CMK-3}$).

2. Experimental

2.1. Catalyst preparation

Rh NP catalysts (Rh/AC and $\text{Rh}/\text{CMK-3}$) with 1 % weight were synthesized by the conventional incipient wetness impregnation method. The preparation process is described as follows: typically, the amorphous coconut activated carbon (AC) was ground to 40–60 mesh, washed with deionized water until the electrical conductivity of the washings was below $20\ \mu\text{S}/\text{cm}$, and then dried in static air at 393 K for 12 h. Subsequently, the support AC and CMK-3 (ordered mesoporous carbon, purchased from Jiangsu Xianfeng Nanomaterial Technology Co. LTD) were impregnated with an aqueous RhCl_3 solution. After drying in an oven at 393 K for 12 h, the as-synthesized catalyst precursor was treated with a three-step procedure: 573 K in Ar (100 ml/min) for 2 h, then 573 K in H_2 (100 ml/min) for 2 h, and finally passivated in 1 % O_2/N_2 (100 ml/min) at ambient temperature.

Single- Rh_1 -site (Rh_1/AC) catalyst was prepared via the atomic dispersive strategy of Rh NP (Rh/AC) according to the method we reported before [27]. The Rh/AC was simply treated with with a mixture of $\text{CO}/\text{CH}_3\text{I}$ (CO passed through a bottle filled with CH_3I at 30 ml/min at room temperature) at 513 K for 2 h. The resulting single- Rh_1 -site (Rh_1/AC) catalyst was obtained and cooled to ambient temperature in a flow of CO .

2.2. Catalyst characterization

To obtain the microscopic structure of the catalysts, the high-resolution transmission electron microscope (**HR-TEM**) images of the samples were obtained with JEM-2100. The aberration-corrected high-angle annular dark-field scanning transmission electron microscopy (**HAADF-STEM**) images were also recorded on a JEM-ARM200F instrument with a CEOS probe corrector working at 200 kV to investigate the atom distribution at a resolution of 0.08 nm.

To obtain the electrical valence of Rh and S atoms, X-ray photoelectron spectroscopy (**XPS**) characterization was performed using a Thermo Fisher ESCALAB 250Xi, equipped with a monochromated $\text{Al K}\alpha$ X-ray source ($h\nu = 1486.6\ \text{eV}$, 15 kV, 10.8 mA). During data collection, the vacuum and the working pressure were limited to $3 \times 10^{-8}\ \text{Pa}$ and $7.1 \times 10^{-5}\ \text{Pa}$, respectively.

To obtain the transformation of H_2S on Rh_1/AC interacted with CH_3OH and/or CH_3I , the in-situ diffuse reflectance infrared Fourier transform spectroscopy (**in-situ DRIFTS**) measurements were conducted on a VERTEX 80 v FTIR spectrometer with a mercury cadmium telluride (MCT) detector cooled by liquid nitrogen. 0.1 g catalyst was loaded into a PIKE high-temperature reaction chamber (ZnSe windows). For each DRIFTS experiment, the catalyst was first calcined in He (20 ml/min) at 573 K for 30 min. Then, the temperature was reduced to 513 K, followed by the introduction of the reaction gas. The mixture of CH_3OH and CH_3I (30 wt% CH_3I) was bubbled by reaction gas (CO , CO/H_2 , He) at 298 K during the reaction, and the FT spectra were recorded between $800\ \text{cm}^{-1}$ to $4000\ \text{cm}^{-1}$ with 64 scans at a resolution of $4\ \text{cm}^{-1}$ to improve the signal to noise ratio.

To obtain the intermediates of the transformation of H_2S to CH_3SCH_3 and CH_3SH on Rh_1/AC during the methanol carbonylation, the in-situ flow-tube free-electron laser time of flight mass spectrometry (**in-situ FEL/TOF MS**) was conducted at the Dalian Coherent Light Source of China [28]. The in-situ formed short-lived intermediate species could also be detected with the same instrument. Experiments on a series of ultraviolet wavelengths, i.e., 112 nm, 115 nm, 118 nm, 125 nm, 140 nm,

and 150 nm, were performed according to the ionization energy of intermediate species. Laser dissociation and laser photoionization/time of flight mass spectrometry (LDI/TOF MS) were also conducted to detect the dissociative fragment of spent Rh₁/AC in normal or H₂S co-feed, and further, identify their mononuclear molecular structure. For the LDI/TOF MS experiments, 266 nm lasers were slightly focused on the sample. The skimmed He atom beam passed the sample surface at a distance of 1 mm to carry the dissociated, then sputtering the species to the detection chamber, and lastly ionized with the free-electron laser.

To obtain the first shell coordination environment of the single-Rh₁-site on Rh₁/AC, the extended X-ray absorption fine structure (EXAFS) data of Rh K-edge were collected at beamline BL14W1 of Shanghai Synchrotron Radiation Facility (SSRF) [29]. 0.20 g sample was ground into 400 meshes and pressed into a small slice with a size of 0.5 cm × 0.5 cm before being mounted to the test site. The data of Rh were recorded in the fluorescence mode equipped with an Electro-Lytle detector. The original EXAFS data of Rh were firstly calibrated by Athena software and then further processed with the Artemis software package. The theoretical scattering amplitude and the phase-shift functions of all the paths for fitting the EXAFS data were calculated with the FEFF6 code. The X-ray absorption near-edge structure (XANES) was also analyzed with the pre-edge (1 s→3d) data of EXAFS to investigate the electronic properties (oxidative state). The wavelet transform was carried out with the software module of FORTRAN, which was developed by Harald Funke and Marina Chukalina [30].

2.3. Density functional theory (DFT) calculation

To investigate the coordination of H₂S, CH₃SH, CH₃SCH₃ with Rh₁/AC, and disclose the sulfur effect on single-Rh₁-site catalyst for methanol carbonylation, DFT was implemented to calculate the relative energy of the coordination of H₂S, CH₃SH, CH₃SCH₃ with Rh₁/AC and the sulfur influence on the energy barrier of the rate-determining step of the oxidative addition of CH₃I on Rh₁/AC.

The activated carbon (AC) model was constructed with a carbonyl group based on the molecule geometry of a Graphene-like structure. All of the molecular structures were optimized by the density functional theory (DFT) using the Vienna ab initio simulation package (VASP). The Perdew-Burke-Ernzerhof (PBE) was used as the exchange-correlation function. The cut-off kinetic energy was set to 420 eV. Brillouin zone integration was approximated using the Monkhorst-Pack k-points method [31] and set as 1 × 1 × 1. The height of the vacuum slab was selected at 12 Å to eliminate the size error. The Geometries were optimized until the energy converged to 1.0 × 10⁻⁴ eV/atom and the force converged to 0.05 eV/Å. Here, it needs to note that the transition states were optimized using the Dimer method, and the energy corrections of van der Waals (vdW) were calculated using the semiempirical approach proposed by Grimme [32] (DFT-D2 method) in conjunction with the PBE functional. All of the stable molecule geometries complexes of Rh₁/AC were checked by the frequency calculations without imaginary frequency, while the transition state structures of Rh₁/AC complexes were checked with one imaginary frequency. In this study, the unit of molecule bond length or distance between atoms was angstrom.

2.4. Catalyst evaluation

The catalytic activity of 1 wt% single-Rh₁-site (Rh₁/AC) catalyst for methanol carbonylation was evaluated in a fixed-bed reactor. 0.3 g catalyst was placed in the center of the Hastelloy C-276 reactor (Ø6 mm × 400 mm). The upper and lower space was filled with quartz sand. Upstream from the reactor, the liquid was vaporized and mixed with CO/H₂ or CO/H₂/H₂S in a Hastelloy tube wrapped with heat tape maintained at 513 K. Generally, the heterogeneous methanol carbonylation reaction was operated under the conditions of 513 K, 1.7 MPa, catalyst 0.1 or 0.3 g, CO 55.4 ml/min or 96.4 ml/min, H₂ 5.5 ml/min or 9.6 ml/min, CH₃OH (liquid) 87.0 µl/min, CH₃I (liquid) 13.0 µl/min. The

tailed gas was chilled at 278 K to collect the liquid product. Incondensable gas was analyzed using online with gas chromatography (Agilent 7890B) equipped with a TCD (chromatographic column: Plot Q), and the collected liquid product was analyzed offline by an FID (chromatographic column: HP-FFAP). The catalytic activity was calculated based on the total moles of acetyl products (CH₃COOH and CH₃COOCH₃) and the total moles of Rh per hour. TOS is the abbreviation of time on stream. CO Conv.% is the conversion of CO. MA. Sel.% is the selectivity of methyl acetate and the HAC. Sel.% is the selectivity of acetic acid. Acetyl products include methyl acetate and acetic acid. The homogeneous methanol carbonylation was implemented at the conditions: 433 K, 0.01 g RhI₃, CO 3.5 MPa, CH₃OH 160 mmol, CH₃I 16 mmol, ultra-pure water 556 mmol, reaction 20 min, 50 ml zirconium autoclave reactor, Conv.% is the conversion of CO.

3. Results

The impact of H₂S on the catalytic activity of Rh NP (Rh/CMK-3) catalyst for methanol carbonylation was investigated in a fixed-bed reactor. As indicated in Fig. 1a and Table S1, Rh/CMK-3 displayed an initial 2530 mol_{CO}/(mole_{Rh}·h) activity in normal feed at 3.7 h and lastly stabilized with the activity of 395 mol_{CO}/(mole_{Rh}·h) at 27.8 h. However, a poor initial activity of 1057 mol_{CO}/(mole_{Rh}·h) was exhibited at 3.3 h and lastly stabilized with the value of only 17 mol_{CO}/(mole_{Rh}·h) at 28.3 h under the conditions containing 1000 ppm H₂S (H₂S co-feed). The result strongly indicates the sulfur poisoning of Rh NP (Rh/CMK-3) by H₂S for methanol carbonylation.

Another Rh NP (Rh/AC) catalyst was also implemented to investigate the influence of H₂S on Rh NPs for methanol carbonylation. As indicated in Fig. 1b and Table S2, the initial activity of Rh/AC is 1128 mol_{CO}/(mole_{Rh}·h) at 0.4 h in a normal feed, and then increased rapidly to 2005 mol_{CO}/(mole_{Rh}·h) at 1.8 h, and lastly stabilized at 2983 mol_{CO}/(mole_{Rh}·h) at 6.1 h. Differently, the initial activity is 1835 mol_{CO}/(mole_{Rh}·h) for Rh/AC in an H₂S co-feed at 0.5 h and lastly stabilized at 3403 mol_{CO}/(mole_{Rh}·h) at 10.7 h.

Single-Rh₁-site (Rh₁/AC) catalyst was conducted to inspect the influence of H₂S. As shown in Fig. 5 and Table S3, the Rh₁/AC catalyst showed an activity value of 3192 mol_{CO}/(mole_{Rh}·h) for 35.9 h in the normal feed condition for methanol carbonylation in a fixed-bed reactor, while the activity could stabilize at 3974 mol_{CO}/(mole_{Rh}·h) for 36.0 h by introducing 1000 ppm H₂S within feedstock stream. A sulfur promotion on an Rh₁/AC catalyst was achieved for methanol carbonylation.

4. Discussions

4.1. Sulfur poisoning on Rh NP catalyst (Rh/CMK)

HAADF-STEM images and EDS elemental mapping showed that the Rh NPs were both clearly dispersed on the CMK-3 support (Fig. 2a-c, and Fig. S1) before and after the reaction in normal or H₂S co-feed. While the mean particle diameter of the spent Rh/CMK-3 grew up from 1.55 ± 0.04 to 3.34 ± 0.09 nm in the normal feed or 3.49 ± 0.11 nm in the H₂S co-feed, respectively. The growth of Rh NP in Rh/CMK-3 corresponds to the reduced carbonylation activity. STEM-EDS line scanning profiles of a single NP in fresh Rh/CMK-3 showed a pure Rh metal and a faint O signal (Fig. 3a, d). The faint O signal should originate from the oxide passivation layer produced during exposure to air for sample handling. Meanwhile, besides the linear scanning profile of the Rh signal, stronger O and weaker I signals appeared on the Rh NP of spent Rh/CMK-3 in normal feed (denoted as Rh/CMK-3-R) (Fig. 3b, e). The stronger O signal may arise from the chemisorbed acetyl product (methyl acetate and acetic acid) on the surface of Rh NPs. Moreover, a stronger S signal appeared for the spent Rh/CMK-3 in the H₂S co-feed (denoted as Rh/CMK-3-SR), and its variation trend was similar to that of the Rh signal (Fig. 3c, f), which apparently demonstrated the formation of Rh-S passivation layer on the Rh NP of Rh/CMK-3-SR.

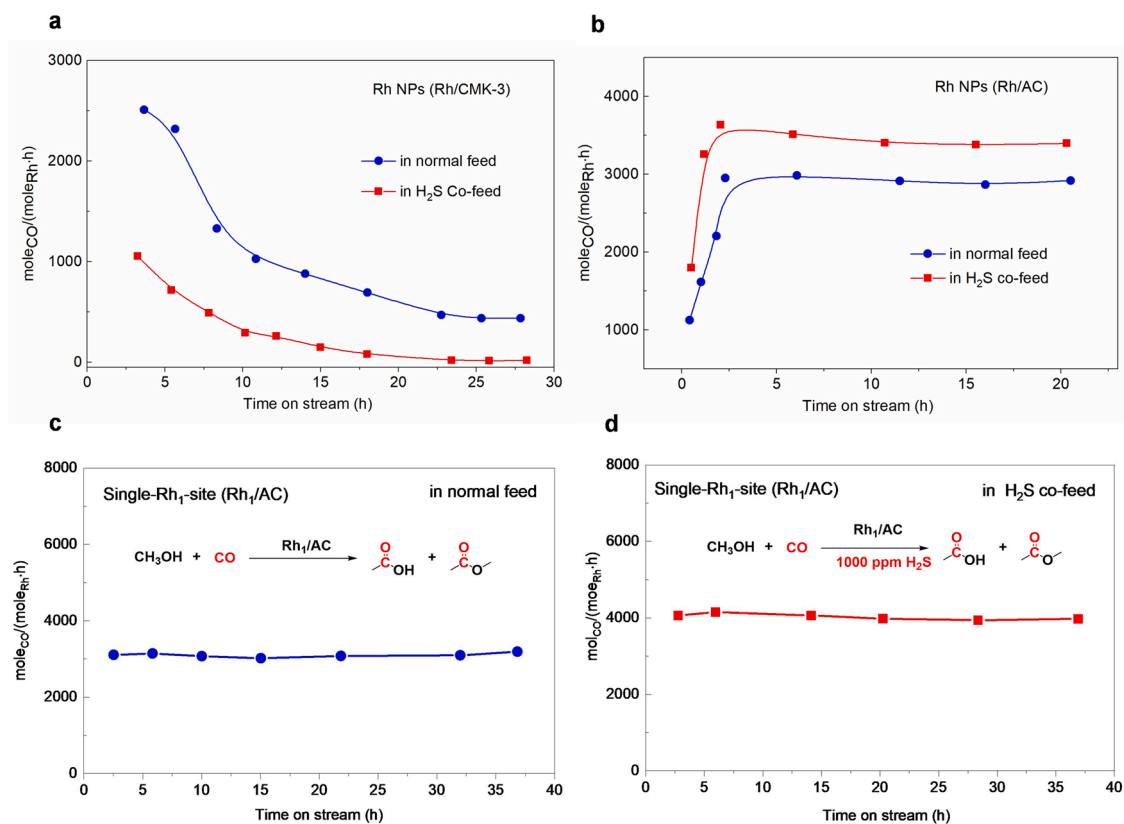


Fig. 1. Impact of H_2S on the activity of Rh NPs (Rh/CMK-3 and Rh/AC) and single-Rh₁-site (Rh₁/AC) for methanol carbonylation. Conditions: H_2S co-feed, H_2S 1000 ppm in syngas (CO/H_2), 513 K, 1.7 MPa, $\text{CO}/\text{CH}_3\text{OH}=1.0$ (mole ratio), $\text{CO}/\text{H}_2=10$ (molar ratio), $\text{CH}_3\text{I}/\text{CH}_3\text{OH}=3/7$ (mass ratio), CO 55.4 ml/min, H_2 5.5 ml/min, CH_3OH (liquid) 87.0 $\mu\text{l}/\text{min}$, CH_3I (liquid) 13.0 $\mu\text{l}/\text{min}$, 0.3 g Rh/AC or Rh/CMK-3 or Rh₁/AC in a $\varnothing 6\text{ mm} \times 400\text{ mm}$ Hastelloy fixed-bed reactor.

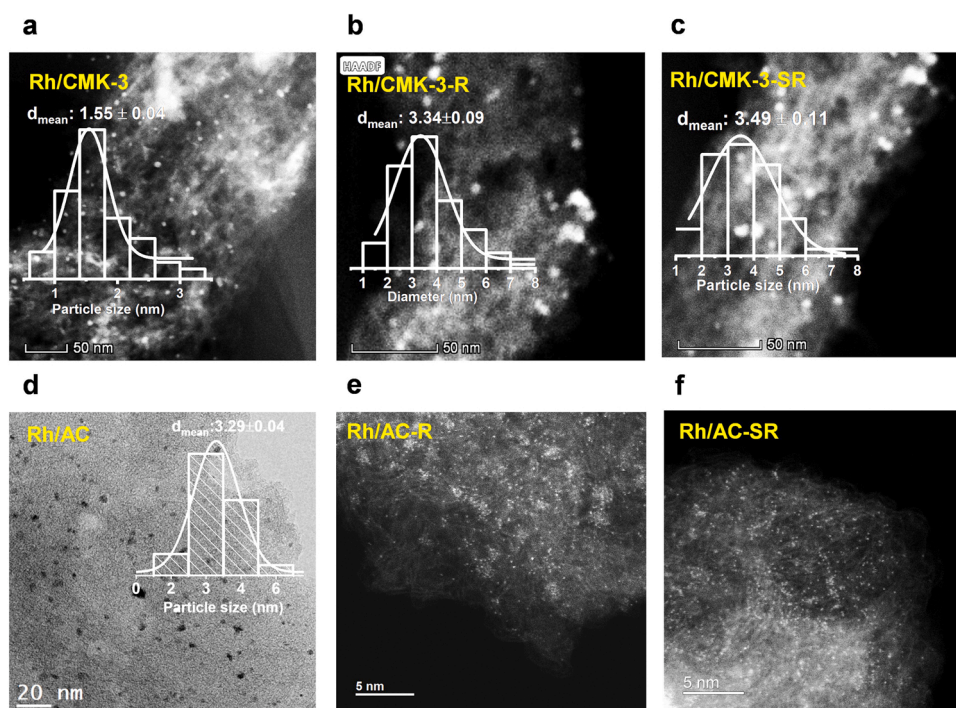


Fig. 2. HAADF-STEM images of fresh Rh NPs (Rh/CMK-3 and Rh/AC), spent Rh NPs in normal feed (Rh/CMK-3-R and Rh/AC-R), and spent Rh NPs in H_2S co-feed (Rh/CMK-3-SR and Rh/AC-SR).

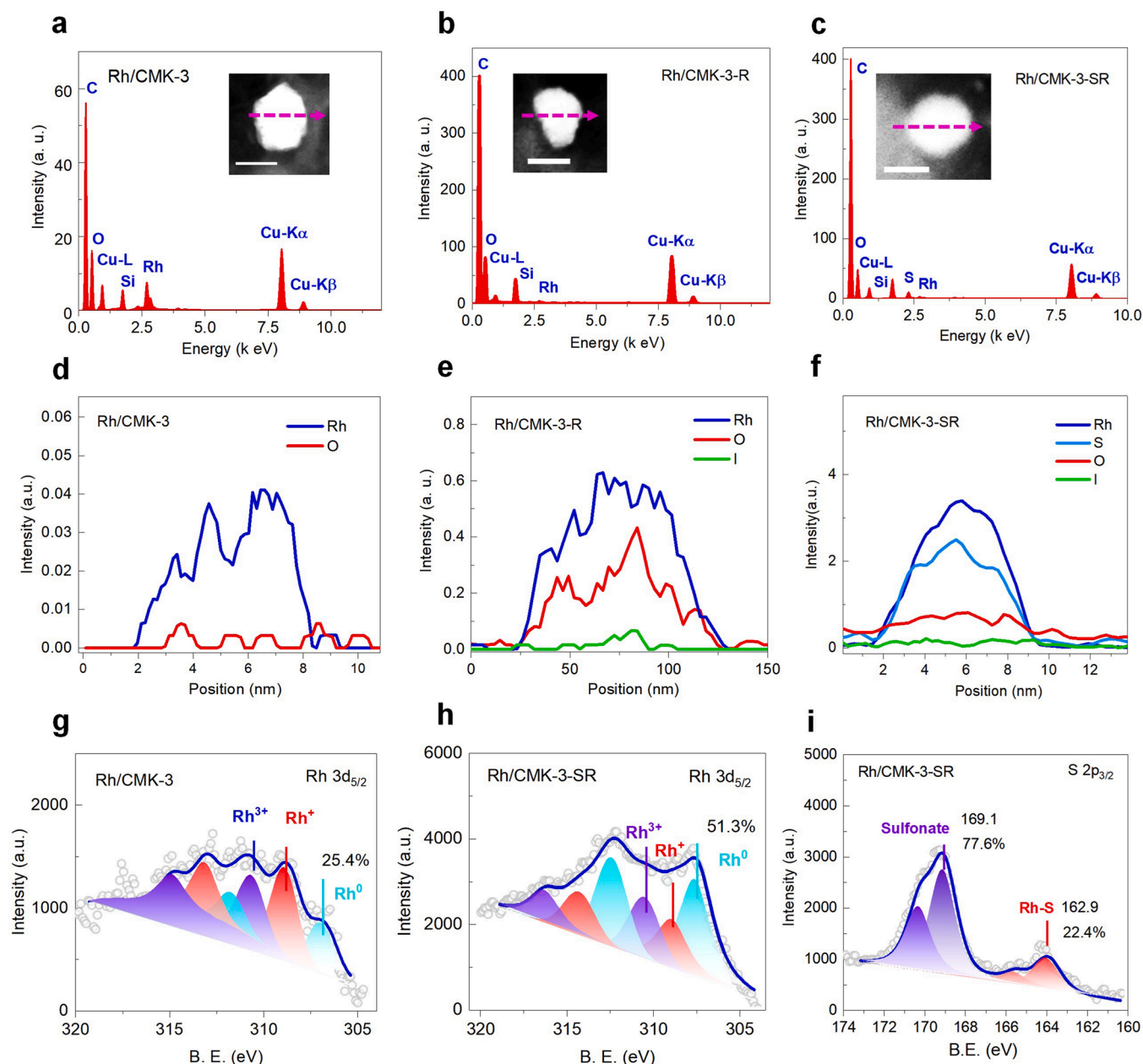


Fig. 3. STEM-EDS line scanning and XPS analysis of Rh NPs (Rh/CMK-3, Rh/CMK-3-R, and Rh/CMK-3-SR). STEM-EDS line scan profiles of a single NP of (a) Rh/CMK-3, (b) Rh/CMK-3-R, and (c) Rh/CMK-3-SR. EDS analysis of (d) Rh/CMK-3, (e) Rh/CMK-3-R, and (f) Rh/CMK-3-SR. XPS analysis of (g) Rh 3d_{5/2} of Rh/CMK-3, (h) Rh/CMK-3-R, and (i) S 2p_{3/2} of Rh/CMK-3-SR.

Additionally, the Rh 3d_{5/2} profile of Rh/CMK-3-SR showed 51.3 % Rh⁰, 24.8 % Rh⁺, and 23.9 % Rh³⁺, while it was 25.4 % Rh⁰, 43.8 % Rh⁺, and 30.8 % Rh³⁺ for Rh/CMK-3-R (Fig. 3g-h, and Table S4). Rh⁰ was the inactive electronic state for the carbonylation reaction. The S 2p_{3/2} spectrum displayed two characteristic peaks at 162.9 eV (22.4 %) and 169.1 eV (77.6 %) (Fig. 3i), which belonged to Rh-S and sulfonate of support, respectively [33]. No H₂S signal (170.7 eV) was detected [33], further evidencing the formation of an Rh-S layer on the surface of Rh NPs. The formed Rh-S passivation layer would elevate the binding energy of Rh⁰ from 306.8 eV to 307.4 eV for their electronic interaction, blocking the adsorption of new reactants, leading to catalyst deactivation, and sulfur poisoning in H₂S co-feed. It is similar to the sulfur poisoning of metal NPs as previously reported [1–5].

4.2. Different structure evolution of Rh NP (Rh/CMK and Rh/AC)

Different from the growing up and agglomeration of Rh NP of Rh/CMK after the reaction, Rh/AC demonstrated the opposite phenomenon that the Rh NPs atomically dispersed after the reaction. The HR-TEM and HAADF-STEM images of fresh and spent Rh/AC were provided (Fig. 2d-e). It could be found that large amounts of Rh NPs distributed uniformly on the surface of the fresh Rh/AC catalyst, but a lot of single-Rh-atoms were produced after the reaction either in normal feed (denoted as Rh/AC-R) or in H₂S co-feed (denoted as Rh/AC-SR), which clearly indicates that an atomic dispersive process occurred for the Rh NPs during methanol carbonylation. It should be owing to the CO and CH₃I reactants, which could induce the atomic dispersion of Rh NPs and prepare a single-Rh₁-site catalyst [27]. Thus, the H₂S in the feed had little influence on the atomic dispersion of Rh NPs on AC and

unexpectedly possessed a positive effect on the performance of the single-Rh₁-site catalyst.

The different performances of Rh/AC and Rh/CMK-3 during methanol carbonylation should be aroused from the intrinsic physical and chemical characteristics of the support CMK-3 and AC. Although they possessed a comparative surface area, the main porous size distribution of CMK-3 was 2 ~ 6.5 nm, much larger than that of the size 1 ~ 2 nm for AC (Fig. S2). In addition, the surface of AC possessed abundant oxygen-containing groups (>C=O, >C-OH, and -COO-) and the carbonyl (>C=O) group was the most thermal stable, which provides the anchoring sites for the single Rh atoms under high-temperature reaction conditions [21]. While it is absent on the CMK-3 surface [34], the Ostward ripping and agglomeration of metal atoms could happen easily. Therefore, the surface functional group with high stability is vital to maintain the structure and reactivity of single-site metal atoms. As a result, Rh NP supported on mesoporous carbon (Rh/CMK-3) was used as

the model catalyst to investigate the effect of sulfur species on NP for methanol carbonylation.

4.3. Structure and sulfur coordination of Single-Rh₁-Site (Rh₁/AC)

The Rh₁/AC catalyst was prepared via the atomic dispersive strategy of Rh NP (Rh/AC) according to the method we reported before [27]. As shown in Fig. 4a, no obvious nanoparticles existed but a lot of isolated single Rh atoms spread uniformly on the surface of the AC. XANES at the pre-edge (1 s→3d) identified the overall positive electronic valence of the single-Rh-atoms in Rh₁/AC when compared with the metallic reference (Fig. 4b). XPS spectrum of Rh 3d_{5/2} at 309.1 and 311.8 eV consistently suggested the valence of Rh⁺ and Rh³⁺ for the isolated single Rh atoms, compared with the Rh foil (Rh⁰) (Fig. 4c-d). Wavelet transform contour plots also showed the Rh-Rh backscattering peak located at the value of ~9.4 Å⁻¹ for Rh foil, while the Rh-I

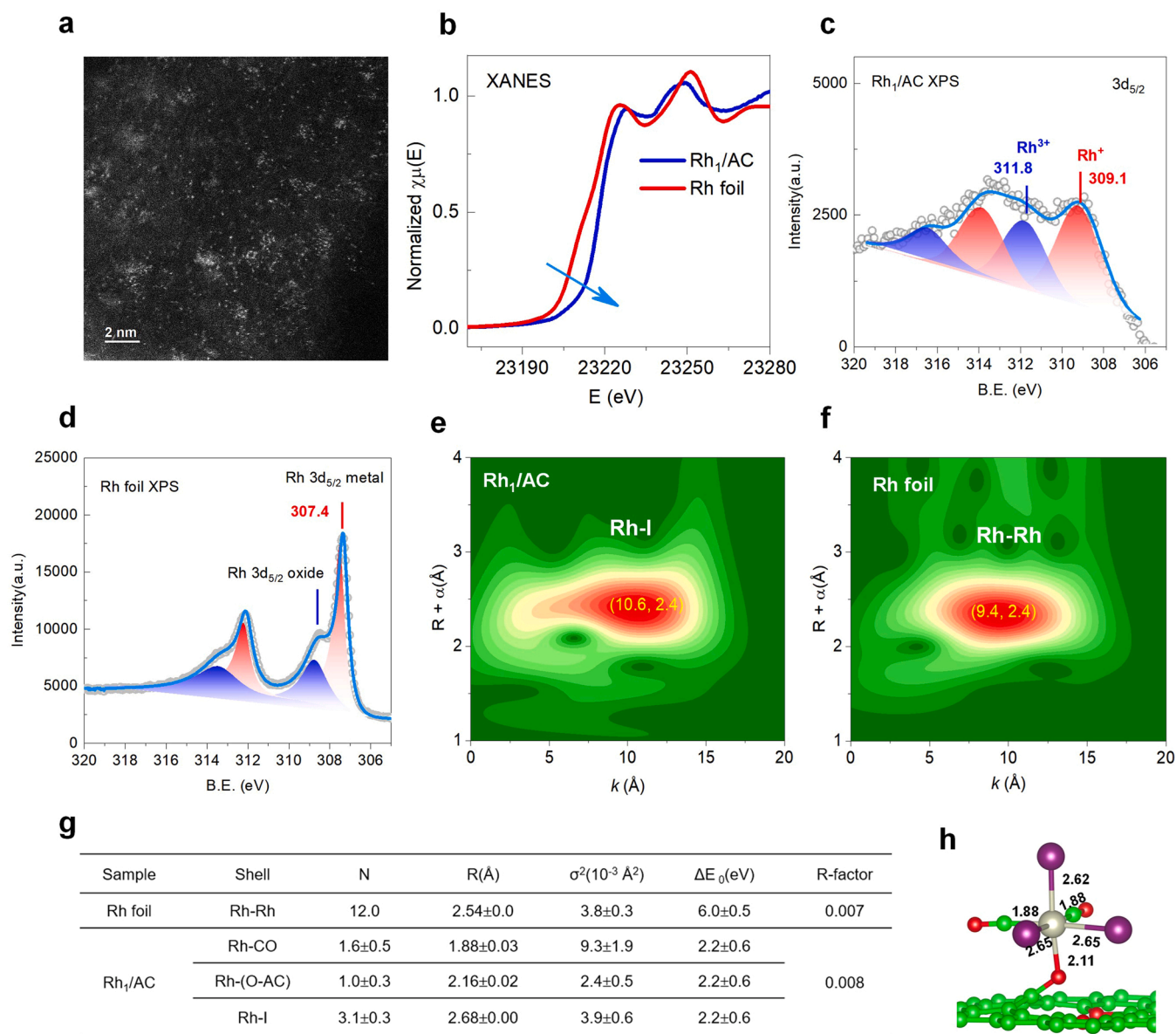


Fig. 4. Characterization of single-Rh₁-site catalyst (Rh₁/AC). (a) HAADF-STEM image of the Rh₁/AC. (b) XANES of the Rh₁/AC and Rh foil. (c) Rh 3d_{5/2} XPS of the Rh₁/AC. (d) Rh 3d_{5/2} XPS of the Rh foil (metal). (e) The wavelet transform contour plots of Rh₁/AC. (f) The wavelet transform contour plots of Rh foil. (g) The scattering paths fitting result of the first shell of Rh atoms in Rh foil and the Rh₁/AC. N, coordination number; R, the distance between absorber and backscatter; σ^2 , Debye-Waller factor; E_0 , energy shift; amp 0.858; k-weight= 1, 2, 3; Feff calculations: Single scattering, Rh-Rh, reference CIF: Reff= 2.539 Å, Rh-CO, reference CIF: [C₄I₂O₄Rh₂], Reff= 1.854 Å, Rh-I, Reff= 2.661 Å, Rh-O, first quick shell path, Reff= 2.1 Å. (h) The molecular model of single-site Rh₁/AC (The green atoms are C, and the red atoms are O, and the brown atoms are I, and the gray atom is Rh. The bond distance are calculated with DFT.).

backscattering peak concentrated at the value of $\sim 10.6 \text{ \AA}^{-1}$ for the Rh_1/AC and no Rh-Rh signal was observed (Fig. 4e-f), further confirming the sole existence of single Rh ions from the viewpoint of electron scattering [35].

The first shell coordination environment of the single- Rh_1 -site in Rh_1/AC was also investigated with EXAFS. The corresponding fitting with imaginary in R space was processed with the data of Rh_1/AC and the metallic Rh foil reference (Fig. S3). For the data of metallic Rh foil, an Rh-Rh path was first fitted with the $\text{Reff}=2.54 \text{ \AA}$. While for the data of Rh_1/AC , the scattering paths of Rh-CO ($\text{Reff}=1.85 \text{ \AA}$), Rh-I ($\text{Reff}=2.66 \text{ \AA}$), and the possible Rh-(O=AC) (O=AC represents carbonyl groups on the surface of AC) were fitted with the coordination number (CN) of 1.6 ± 0.5 , 3.1 ± 0.3 , and 1.0 ± 0.3 , respectively. According to the model of a single nuclear complex $[\text{Rh}(\text{CO})_x\text{I}_y(\text{O}=\text{AC})]$ (Fig. 4g), the O=AC functioned as both the anchor site and ligand on the surface of support AC for immobilizing the single Rh sites [36–38]. The molecular structure of Rh_1/AC here was convincingly identified as the main species of $[\text{Rh}(\text{CO})_2\text{I}_3(\text{O}=\text{AC})]$ (Fig. 4h) following the 16–18e effective atomic number (EAN rule) theory [39].

To probe the sulfur coordination of the single- Rh_1 -site, the spent Rh_1/AC in normal feed (denoted as $\text{Rh}_1/\text{AC-R}$) and H_2S co-feed (denoted as $\text{Rh}_1/\text{AC-SR}$) were systematically investigated. Consistently, the atomic distribution of Rh atoms in $\text{Rh}_1/\text{AC-R}$ and $\text{Rh}_1/\text{AC-SR}$ was still observed by HAADF-STEM images (Fig. 5a-b). The first shell coordination environment of $\text{Rh}_1/\text{AC-R}$ and $\text{Rh}_1/\text{AC-SR}$ were also investigated with EXAFS, and the corresponding fittings in R and k space and its imaginary were presented (Fig. 5c-d, and Fig. S4). For the case of $\text{Rh}_1/\text{AC-R}$, an Rh-I bond at $2.7 \pm 0.0 \text{ \AA}$ with a CN of 2.7 ± 0.2 was the

primary contributor (Table S5). The small peak at $1.9 \pm 0.0 \text{ \AA}$ with a CN of 1.6 ± 0.4 was attributed to Rh-CO, while the peak at $2.1 \pm 0.0 \text{ \AA}$ was ascribed to Rh-(O=AC), which represented a coordination bond between single-site Rh atoms and the carbonyl group (O=AC) on the surface of AC. For the case of $\text{Rh}_1/\text{AC-SR}$, a scattering peak of Rh-SR coordination bond at $2.3 \pm 0.0 \text{ \AA}$ with the CN of 0.8 ± 0.2 was well fitted, referred to the standard structure of $\text{RhCl}_3(\text{SMe}_2)_3$ with the $\text{Reff}_{\text{Rh-S}}=2.335 \text{ \AA}$. Besides, a bond of Rh-I at $2.7 \pm 0.0 \text{ \AA}$ with a CN of 3.4 ± 0.3 and a bond of Rh-CO at $2.0 \pm 0.1 \text{ \AA}$ with a CN of 0.5 ± 0.4 were also elaborated. It was found that part of Rh-CO was replaced by Rh-S in the $\text{Rh}_1/\text{AC-SR}$. Besides, the wavelet transform of the $\text{Rh}_1/\text{AC-SR}$ presented a slight difference from the $\text{Rh}_1/\text{AC-R}$ sample. The wavelet signal of $R + \alpha (\text{\AA})$ was 10.8 \AA for $\text{Rh}_1/\text{AC-R}$ while it was 12.3 \AA for $\text{Rh}_1/\text{AC-SR}$ (Fig. 5e-f). This should be caused by the coordination of CH_3SCH_3 with the single-site Rh atoms as $\text{Rh-S}(\text{CH}_3)_2$. Therefore, we deduced that the Rh atoms were still atomically presented and a sulfur coordination bond of the $\text{Rh-S}(\text{CH}_3)_2$ should exist for $\text{Rh}_1/\text{AC-SR}$.

Laser desorption ionization time-of-flight mass spectrometry (LDI/TOF MS) was also conducted to further elucidate the molecular structure of $\text{Rh}_1/\text{AC-R}$ and $\text{Rh}_1/\text{AC-SR}$ (Fig. 6a-b). The ionized fragments of $m/z = 15$, $m/z = 28$, $m/z = 43$, and $m/z = 127$ were collected from the data of $\text{Rh}_1/\text{AC-R}$, which should be assigned to CH_3^+ , CO^+ , CH_3CO^+ , and I^+ , respectively. While a new fragment of $m/z = 62$ (CH_3SCH_3) was definitely detected from the data of $\text{Rh}_1/\text{AC-SR}$ beside the normal signals. Rh $3d_{5/2}$ XPS analysis of $\text{Rh}_1/\text{AC-R}$ and $\text{Rh}_1/\text{AC-SR}$ demonstrated a virtually unanimous conclusion with the Rh_1/AC , in which the single-site Rh atoms were still presented as Rh^+ and Rh^{3+} (Fig. 6c-b, and Table S6). But interestingly, a new characteristic peak of S $2p_{3/2}$ at

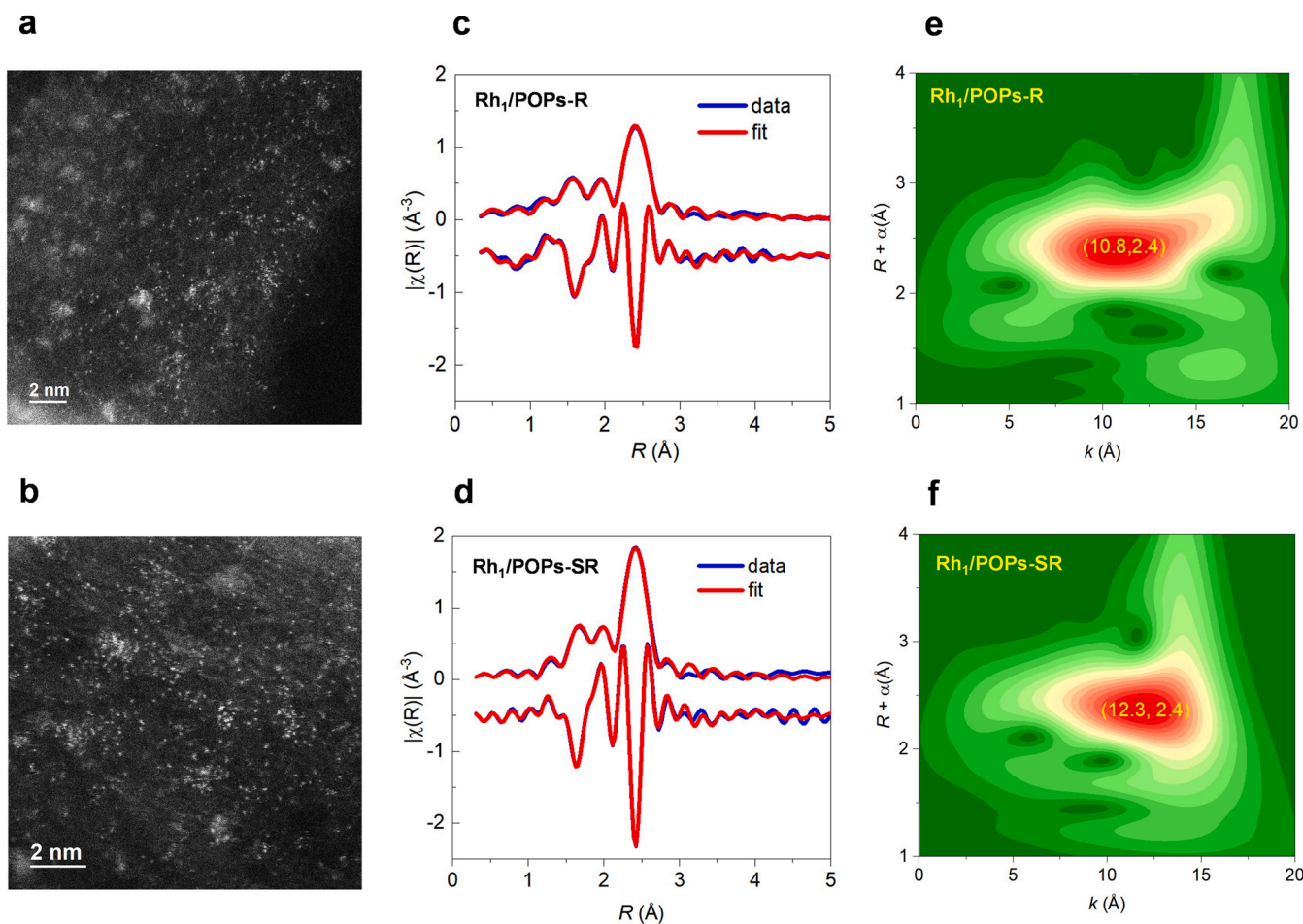


Fig. 5. Characterization of $\text{Rh}_1/\text{AC-R}$ and $\text{Rh}_1/\text{AC-SR}$. HAADF-STEM image of (a) $\text{Rh}_1/\text{AC-R}$, and (b) $\text{Rh}_1/\text{AC-SR}$. R space and its imaginary fitting of Rh K-edge EXAFS of (c) $\text{Rh}_1/\text{AC-R}$, and (d) $\text{Rh}_1/\text{AC-SR}$. (e) and (f) are the wavelet transform contour plots of $\text{Rh}_1/\text{AC-R}$ and $\text{Rh}_1/\text{AC-SR}$, respectively.

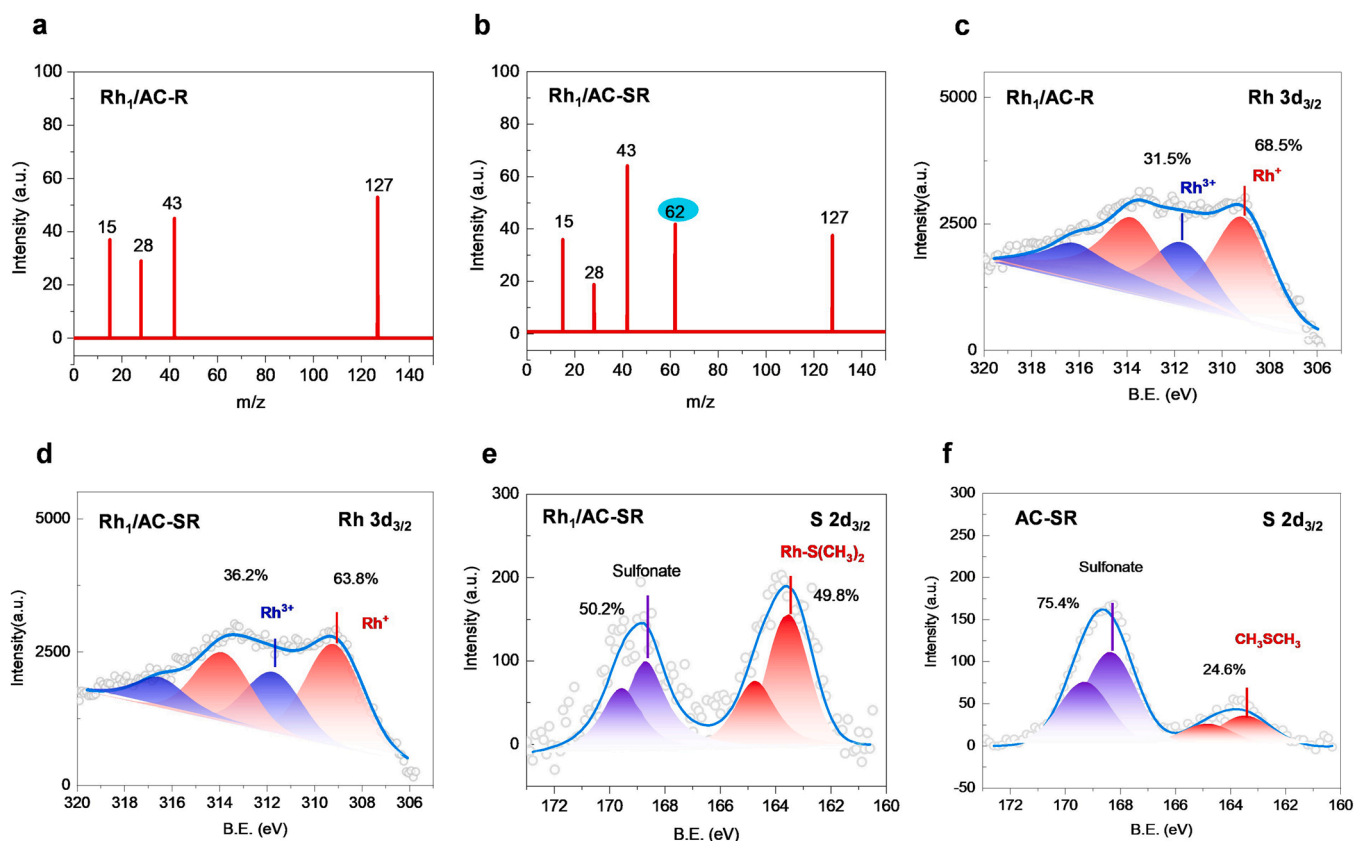


Fig. 6. LDI/TOF MS and XPS of $\text{Rh}_1/\text{AC-R}$ and $\text{Rh}_1/\text{AC-SR}$. LDI/TOF MS analysis of the fragments of (a) $\text{Rh}_1/\text{AC-R}$, and (b) $\text{Rh}_1/\text{AC-SR}$. (c) and (d) are the $\text{Rh } 3d_{3/2}$ XPS of $\text{Rh}_1/\text{AC-R}$ and $\text{Rh}_1/\text{AC-SR}$, respectively. (e) and (f) are the $\text{S } 2d_{3/2}$ XPS of $\text{Rh}_1/\text{AC-SR}$ and AC-SR , respectively. (The gray cycles were the original data and the blue line was the fitting envelope curve, and the red peaks in (c) and (d) are Rh^+ species of $3d_{5/2}$ (309.1 eV) and $3d_{3/2}$, respectively. The blue peaks in (c) and (d) are Rh^{3+} species of $3d_{5/2}$ (311.8 eV) and $3d_{3/2}$, respectively. The red peaks in (e) were the fitting peaks were attributed to the $\text{S } 2p_{3/2}$ (163.4 eV) and $3d_{3/2}$, respectively. The purple peaks were attributed to the sulfonate in $\text{S } 2p_{3/2}$ (168.5 eV) and $2p_{1/2}$, respectively).

163.4 eV, probably ascribed to CH_3SCH_3 [40,41], was detected for $\text{Rh}_1/\text{AC-SR}$ when compared with blank data of AC-SR (Fig. 6e-f, and Table S6). It agreed well with the result of LDI/TOF MS of $\text{Rh}_1/\text{AC-SR}$, in which a new $m/z = 62$ (CH_3SCH_3) fragment was detected, and the results of EXAFS and XANES. Thus, a coordination molecular structure of $(\text{CH}_3\text{-SR})\text{Rh}(\text{CO})\text{I}_3(\text{O}=\text{AC})$ ($\text{R}=\text{H}, \text{CH}_3$) was proposed to in-situ generate on the Rh_1/AC .

4.4. Transformation of H_2S into organic CH_3SCH_3 and CH_3SH on Rh_1/AC

In-situ DRIFTS experiments were also executed to investigate the transformation of H_2S on the Rh_1/AC for methanol carbonylation. As indicated in Fig. 7a-b, and Fig. S5, the adsorption of CO (2120 and 2170 cm^{-1}) [42], CH_3OH (1004 and 1060 cm^{-1}) [43], and CH_3I (1234 and 1263 cm^{-1}) [44] on the Rh_1/AC reached equilibrium more rapidly in H_2S co-feed than that in normal feed, which is probably due to the competitive adsorption of sulfur species on single-Rh-site. Besides, the peak at 1780 cm^{-1} was attributed to the acetyl products [45]. It could be found that the carbonylation activity of the Rh_1/AC was not restrained in the H_2S co-feed, and the acetyls products (1780 cm^{-1}) emerged earlier in the H_2S co-feed than that in the normal feed. In addition, the group peaks at $\sim 2984 \text{ cm}^{-1}$ in Fig. 7c should belong to the signals of $\nu(\text{C-H})$ of methyl or its radical signals from CH_3I (Fig. S5). However, this kind of methyl group at $\sim 2984 \text{ cm}^{-1}$ was dramatically attenuated after co-feeding H_2S (Fig. 7d), endorsing the transformation of H_2S to form CH_3SCH_3 or CH_3SH species via a path of methyl radical [46].

To further determine the evolution process of H_2S transformation during reaction, in-situ FEL TOF-MS experiments of methanol

carbonylation were conducted in normal or H_2S co-feed at the Dalian Coherent Light Source of China [47,48]. As indicated in Fig. 8a-b, some new species emerged at $m/z = 33, 34, 47, 48$, and 62 on the Rh_1/AC catalyst after the H_2S co-feed. According to the relationship of molar mass and m/z of the corresponding characteristic peak, whose species should be ascribed to the species of -SH , H_2S , $\text{CH}_3\text{-S}$, CH_3SH , and CH_3SCH_3 . More comparative trials with different ultraviolet wavelengths further determined that the species of $m/z = 62$ and $m/z = 48$ were the CH_3SCH_3 and CH_3SH , respectively (Fig. S6). Because the ionization energy of CH_3SH is 131.9 nm and the signals of $m/z = 48$ vanished when the ultraviolet wavelength was 140 nm , while the ionization energy of CH_3SCH_3 is 144.2 nm and the signals of $m/z = 62$ could not be detected when the ultraviolet wavelength was 150 nm . The species at $m/z = 33, 34$, and 47 should be assigned to -SH , H_2S , and -SCH_3 species, respectively. Besides, the signal of $m/z = 15$ ($\text{CH}_3\cdot$) in the H_2S co-feed was dramatically consumed (Fig. 8a-b), while the signal of $m/z = 127$ ($\text{I}\cdot$) became stronger than those in the normal feed, strongly suggesting a methylation process of H_2S with CH_3I and/or CH_3OH to form CH_3SCH_3 and/or CH_3SH components on Rh_1/AC .

Hence, through the thorough investigation mentioned above, a simple evolution process of H_2S transformation was proposed, in which CH_3I was homolytically cleaved into the radicals of $\text{CH}_3\cdot$ and $\text{I}\cdot$ at the first stage ($\text{CH}_3\text{I} \rightarrow \text{CH}_3\cdot + \text{I}\cdot$), and then the $\text{CH}_3\cdot$ reacted with H_2S to form the $\text{CH}_3\text{S}\cdot$ and $\text{H}\cdot$ ($\text{CH}_3\cdot + \text{H}_2\text{S} \rightarrow \text{CH}_3\text{S}\cdot + \text{H}\cdot$), and further lead to the formation of CH_3SCH_3 ($\text{CH}_3\cdot + \text{CH}_3\text{S}\cdot \rightarrow \text{CH}_3\text{SCH}_3$). The $\text{H}\cdot$ could react with $\text{I}\cdot$ to form HI ($\text{H}\cdot + \text{I}\cdot \rightarrow \text{HI}$), which was approved and HI species ($m/z = 128$) was detected by the in-situ TOF MS. Besides, HI could also react with CH_3OH to form CH_3I and H_2O . The transformation of H_2S to CH_3SCH_3 with temperature function was also depicted (Fig. 8c). The signal

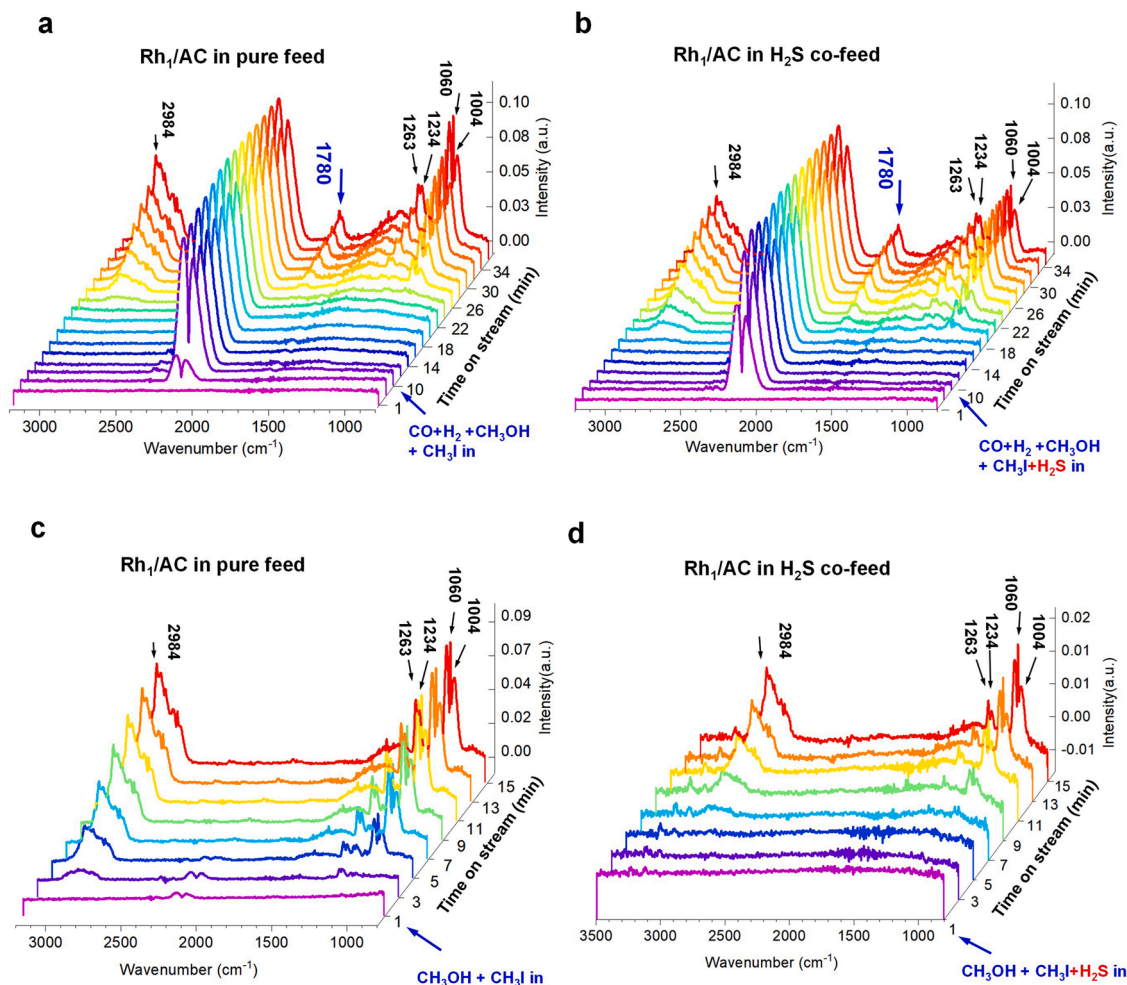


Fig. 7. The in-situ DRIFTS of methanol carbonylation on Rh₁/AC in normal and H₂S co-feed. *In-situ* DRIFTS methanol carbonylation on Rh₁/AC (a) in normal feed, (b) in H₂S co-feed, (c) CH₃OH and CH₃I (d) CH₃OH, CH₃I, and H₂S.

intensity of CH₃SCH₃ ($m/z = 62$) appeared at 373 K and increased the temperature up to 453 K, while the signal intensity of H₂S ($m/z = 34$) decreased rapidly from 313 to 433 K. It further established the intimate relationship of H₂S with CH₃SCH₃.

In addition, comparative experiments under the absence of Rh₁/AC showed that the transformation of H₂S to CH₃SCH₃ via the interaction between H₂S and CH₃OH or CH₃I was feasible at 513 K (Fig. 8d-f), while the transformation of H₂S to CH₃SH needed the assistance of Rh₁/AC. The thermodynamic calculation suggested that the CH₃SCH₃ formation was an exothermic process while the CH₃SH formation was an endothermic process (Table S7) when H₂S reacted with CH₃I. The standard Gibbs formation energy of CH₃SCH₃ was 2.71 kJ/mol, almost one-third of that of CH₃SH (9.25 kJ/mol), further confirming the preferential formation of CH₃SCH₃ from H₂S.

4.5. Theoretical investigation of sulfur coordination on Rh₁/AC

The coordination effects of H₂S, CH₃SH, and CH₃SCH₃ on the single-Rh-site in Rh₁/AC were investigated with the density functional theory (DFT) calculations. The molecular models of (H₂S)Rh(CO)I₃(O=AC), (CH₃SH)Rh(CO)I₃(O=AC), and (CH₃SCH₃)Rh(CO)I₃(O=AC) were constructed and optimized with DFT, and the relative potential energy to Rh(CO)₂I₃(O=AC), which was marked as 0.0 kcal/mol, was 3.5, -9.2 and -14.9 kcal/mol, respectively (Fig. S7). It suggested that the newly formed CH₃SH and CH₃SCH₃ species from H₂S benefit the single-Rh-site in Rh₁/AC to get a more stable mononuclear complex structure.

Moreover, the bond length of CH₃-I in the molecular structure of [I-CH₃-(SR)Rh(CO)I₂(O=AC)] (SR = CH₃SH or CH₃SCH₃) was 2.15 Å, slightly longer than that of 2.13 Å in [I-CH₃-Rh(CO)₂I₂(O=AC)] (Fig. S8), corresponding to the lower chemical energy of CH₃I adsorption on the mononuclear complex after the coordination of CH₃SH and CH₃SCH₃.

In terms of the methanol carbonylation reaction to produce acetic acid (CH₃OH + CO → CH₃COOH) or methyl acetate (2CH₃OH + CO → CH₃COOCH₃ + H₂O), CH₃I was a crucial co-catalyst, participated in the reaction and regenerated after reaction (① CH₃I + CO → CH₃COI, ② CH₃COI + CH₃OH → CH₃COOCH₃ + HI, ③ HI + CH₃OH → CH₃OH + H₂O). Importantly, the oxidative addition of CH₃I to [Rh(CO)₂I₂]⁻ was determined as the rate-determining step [21, 25, 49–53]. CH₃COI was the key intermediate species and the corresponding standard Gibbs formation energy was 121.0 kJ/mol. In comparison, the reaction of CH₃COI with CH₃OH to produce CH₃COOCH₃ and HI was thermal spontaneous and the standard Gibbs formation energy was -160.2 kJ/mol. In addition, the reaction of HI with CH₃OH to produce CH₃I and H₂O was also thermal spontaneous and the standard Gibbs formation energy was -51.9 kJ/mol. Therefore, it is key to investigate the coordination influence of those sulfur species (H₂S, CH₃SH, CH₃SCH₃) on the reaction barrier of the oxidative addition of CH₃I and the subsequent formation of CH₃COI on Rh₁/AC.

The transitional state energy barrier of the oxidative addition of CH₃I was 16.1 kcal/mol for Rh₁/AC according to the normal DFT calculation, higher than those of the subsequent step of CO migration insertion to form CH₃CO (14.6 kcal/mol) and the last step of reductive

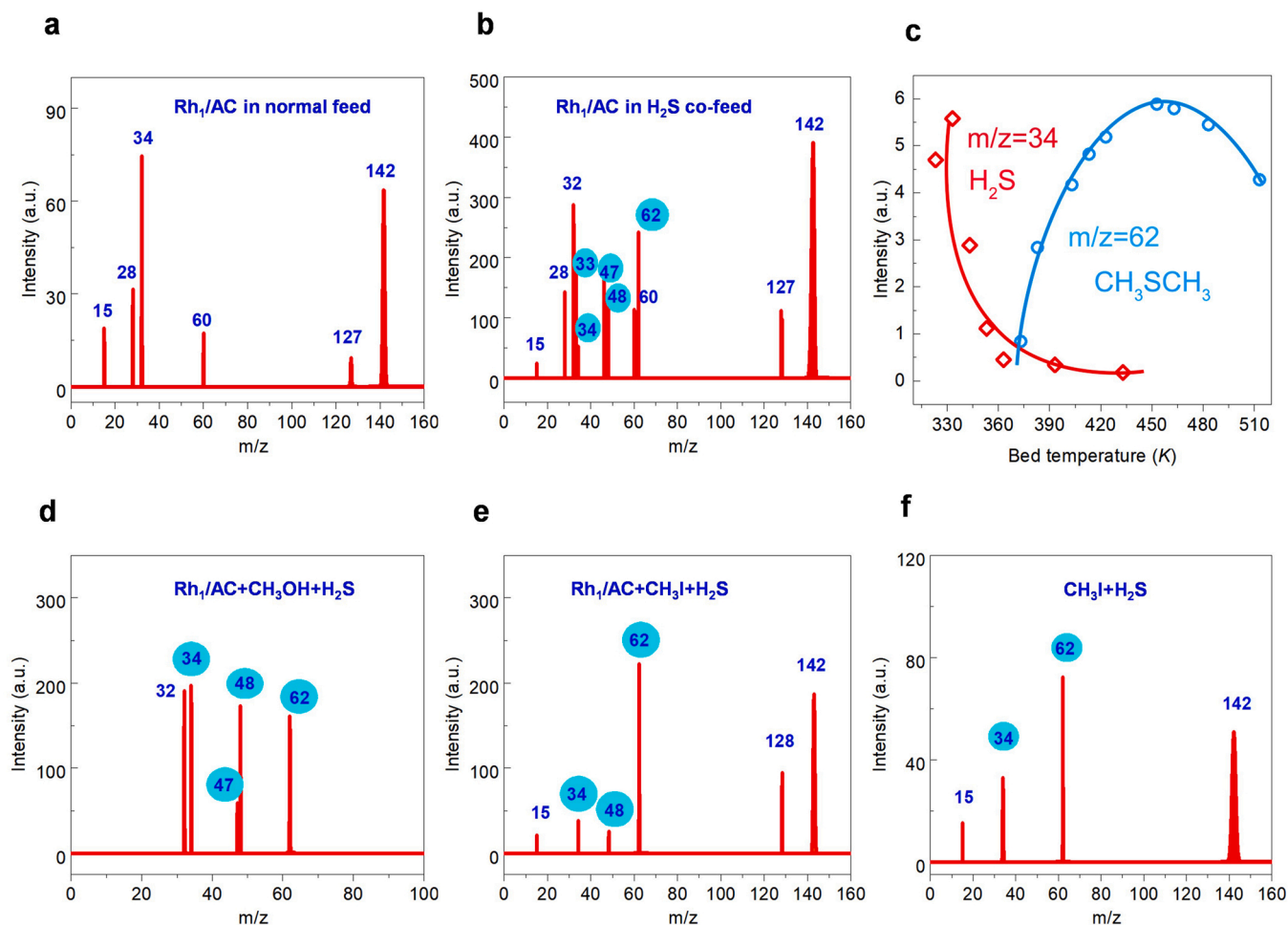


Fig. 8. The in-situ FEL/TOF-MS of methanol carbonylation on Rh₁/AC in normal feed, in H₂S co-feed, and comparative experiments. The in-situ free-electron laser time of flight mass spectrum (FEL/TOF MS) of methanol carbonylation on Rh₁/AC catalyst in (a) normal feed and (b) H₂S co-feed at 513 K, 0.1 bar, FEL 112 nm and 40 μJ/cm², H₂S 10,000 ppm. (c) The normalized signal intensity of *m/z* 34 (H₂S) and *m/z* 62 (CH₃SCH₃) as a function of temperature at the condition of (b). (d) The comparative FEL/TOF MS experiment on Rh₁/AC catalyst with CH₃OH and H₂S. (e) The comparative FEL/TOF MS experiment on Rh₁/AC catalyst with CH₃I and H₂S. (f) The comparative FEL/TOF MS experiment only with CH₃I and H₂S.

elimination of CH₃COI (13.4 kcal/mol), further suggested the rate-determining step of CH₃COI formation on Rh₁/AC was the oxidative addition of CH₃I. For the sulfur effect on the CH₃COI formation on Rh₁/AC, as indicated in Fig. 9 and Fig. S9, a sulfur coordinated structure of [(CH₃SR)Rh(CO)I₂(O=AC)] (R=H, or CH₃) was considered as the initial active site. The transitional state energy barriers for CH₃I oxidative addition of those structures were estimated to be 10.0, 10.5, and 16.5 kcal/mol, when the SR ligand of [I-CH₃-(SR)Rh(CO)I₂(O=AC)][#] separately changed to CH₃SCH₃, CH₃SH, and H₂S respectively (Fig. 9, Fig. S9). While it was 16.1 kcal/mol for [I-CH₃-Rh(CO)I₂(O=AC)][#] according to the DFT calculation. It is easy to find that the coordination of CH₃SCH₃ or CH₃SH with the single-Rh-site could benefit Rh₁/AC catalyst to get a lower energy barrier of CH₃I oxidative addition in theory. Then, the CH₃COI formation was promoted and the carbonylation rate was reasonably increased.

Therefore, the transformation of H₂S into CH₃SCH₃/CH₃SH is crucial for the single-site Rh₁/AC catalyst to gain a sulfur-promoted effect for heterogeneous methanol carbonylation. Nevertheless, a higher concentration of H₂S like 10,000 ppm or 50,000 ppm was harmful, because a large amount of CH₃SCH₃ would lead to another secondary reaction with CH₃I to form a new species of (CH₃)₃SI, which is a white crystal powder, very hard to be dissolved in methanol, resulting in the pore blockage of the catalyst and the piping of the reaction unit.

5. Conclusions

In summary, a role reversal of sulfur from poisoning to a resistant reagent or further promoter was realized for methanol carbonylation via the quick transformation of H₂S to CH₃SH and CH₃SCH₃ by CH₃I and/or CH₃OH. Besides, a sulfur-poisoning on Rh NP (Rh/CMK-3) but sulfur-promotion on its single-Rh-site (Rh₁/AC) was also presented. Interestingly, another Rh NP (Rh/AC) experienced a process of atomic dispersion in heterogeneous methanol carbonylation due to the interaction of CO/CH₃I. Single-Rh₁-site (Rh₁/AC) was thereafter prepared with the atomic dispersive method and performed high sulfur tolerance and even sulfur-promoted carbonylation activity for heterogeneous methanol carbonylation in 1000 ppm H₂S co-feed. The experimental and theoretical DFT calculations demonstrated that the newly formed CH₃SH and CH₃SCH₃ species from H₂S benefit the single-Rh-site (Rh₁/AC) to get a more stable mononuclear complex structure. Besides, CH₃SCH₃ or CH₃SH coordination with the single-Rh-site could benefit Rh₁/AC to get a lower energy barrier of CH₃I oxidative addition and promote the methanol carbonylation. Meanwhile, strong adsorption of sulfur species on Rh NPs formed an isolated Rh-S layer, blocking the adsorption of reactants and leading to sulfur poisoning. The study provides a new perspective to solve the problem of sulfur poisoning of metal catalysts.

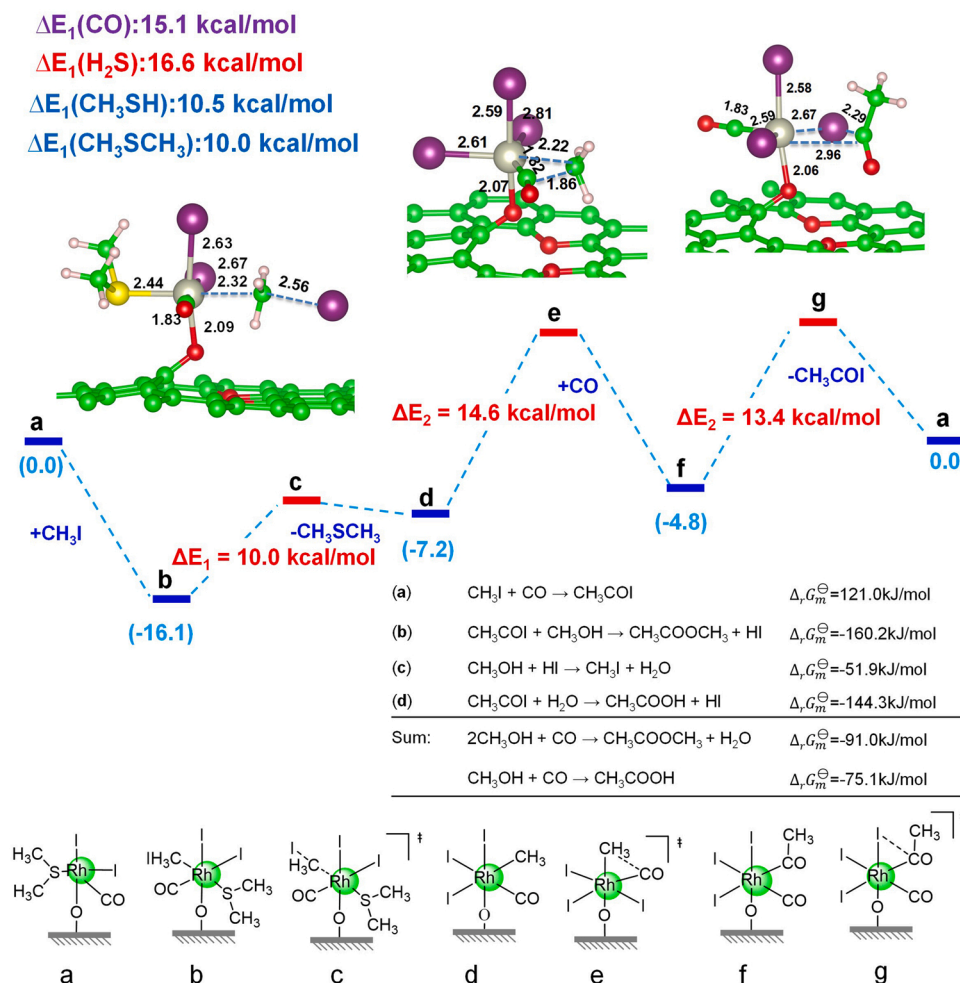


Fig. 9. The DFT calculations about the coordination effect of H₂S, CH₃SH, and CH₃SCH₃ on the potential energy barrier of CH₃I oxidative addition on Rh₁/AC, and the energy evolution during the heterogeneous methanol carbonylation. The gray ball represents the O atom; the purple ball represents the I atom; the yellow ball represents the S atom; the green ball represents the C atom; the pink ball represents the H atom. The Gibbs formation energy was calculated under 298 K.

CRediT authorship contribution statement

S. Feng conceived the project, devised experiments, conducted experiments, collected the data and processed it, and wrote the manuscript; **J. Mu** prepared the materials, conducted experiments, collected the data and analyzed, and participated in the discussion; **X. Lin** performed the theoretical calculations; **X. Song** and **Y. Ding** conceived the project, discussion and revised the manuscript; **S. Liu**, **W. Zhang**, **G. Wu**, **J. Yang**, **W. Dong**, **X. Yang** assisted in conducting the experiments of in-situ FEL/TOF MS; **W. Shi** helped to revise the manuscript; **J. Li** provide much advice on the project and **Z. Jiang** assisted in the experiment of EXAFS test and data processing.

Declaration of Competing Interest

The authors declare that they have no known competing financial interests or personal relationships that could have appeared to influence the work reported in this paper.

Data availability

Data will be made available on request.

Acknowledgements

The financial support for this work by the National Natural Science Foundation of China (22002156, 22108275, and 22288201), the Youth Innovation Promotion Association of the Chinese Academy of Sciences

(2022179), the innovation fund of DICP I202237, the CAS Project for Young Scientists in Basic Research (YSBR-022), the Strategic Priority Research Program of the Chinese Academy of Sciences (No. XDA21020300, No. XDB17020400, and No. XDA29040400), the International Partnership Program of the Chinese Academy of Sciences (No. 121421KYSB20170012), the Key Technology Team of the Chinese Academy of Sciences (Grant No. GJJSTD20190002), the Chemical Dynamics Research Center Grant No. 21688102, the Strategic Priority Research Program of the Chinese Academy of Sciences (Grant No. XDB17000000), the Natural Science Foundation of Zhejiang Province (LY18B060007), the Chinese Academy of Sciences (GJJSTD20220001) and Key Laboratory of Yarn Materials Forming and Composite Processing Technology, Zhejiang Province, China. This research used resources from the Dalian Coherent Light Source. We also sincerely thank Dr. Olga Safonova and Prof. Maarten Nachtegaal for their help in the EXAFS measurements and discussion, and thanks Dr. Jin Cui and Dr. Shuwen Yu for their help in the characterization of XPS, and in-situ FT-IR spectra.

Appendix A. Supporting information

Supplementary data associated with this article can be found in the online version at [doi:10.1016/j.apcatb.2022.122318](https://doi.org/10.1016/j.apcatb.2022.122318).

References

- [1] Y. Zhang, P. Glarborg, M.P. Andersson, K. Johansen, T.K. Torp, A.D. Jensen, J. M. Christensen, Sulfur poisoning and regeneration of Rh-ZSM-5 catalysts for total oxidation of methane, *Appl. Catal. B Environ.* 277 (2020), 119176.

- [2] W. Zhou, W.L. Teo, S.Z.F. Phua, S. Xi, B. Chen, D. Jana, D. Wang, C. Qian, H. Wang, H. Zhang, Y. Zhao, Impeding catalyst sulfur poisoning in aqueous solution by metal-organic framework composites, *Small Methods* 4 (2020), 1900890.
- [3] A. Väliheikki, M. Kärkkäinen, M. Honkanen, O. Heikkinen, T. Kolli, K. Kallinen, M. Huhtanen, M. Vippola, J. Lahtinen, R.L. Keiski, Deactivation of Pt/SiO₂-ZrO₂ diesel oxidation catalysts by sulphur, phosphorus and their combinations, *Appl. Catal. B Environ.* 218 (2017) 409–419.
- [4] H. Häkkinen, The gold–sulfur interface at the nanoscale, *Nat. Chem.* 4 (2012) 443–455.
- [5] K. Chu, Q.-Q. Li, Y.-P. Liu, J. Wang, Y.-H. Cheng, Filling the nitrogen vacancies with sulphur dopants in graphitic C₃N₄ for efficient and robust electrocatalytic nitrogen reduction, *Appl. Catal. B Environ.* 267 (2020), 118693.
- [6] C.H. Bartholomew, P.K. Agrawal, J.R. Katzer, Sulfur poisoning of metals, *Adv. Catal.* 31 (1982) 135–242.
- [7] S.A. Theofanidis, J.A.Z. Pieterse, H. Poelman, A. Longo, M.K. Sabbe, M. Virginie, C. Detavernier, G.B. Marina, V.V. Galvita, Effect of Rh in Ni-based catalysts on sulfur impurities during methane reforming, *Appl. Catal. B Environ.* 267 (2020), 118691.
- [8] D.E. Doronkin, S. Fogel, S. Tamm, L. Olsson, T.S. Khan, T. Bligaard, P. Gabrielsson, S. Dahl, Study of the “Fast SCR”-like mechanism of H₂-assisted SCR of NO_x with ammonia over Ag/Al₂O₃, *Appl. Catal. B Environ.* 113 (2012) 228–236.
- [9] L. Liu, A. Corma, Metal catalysts for heterogeneous catalysis: from single atoms to nanoclusters and nanoparticles, *Chem. Rev.* 118 (2018) 4981–5079.
- [10] H. Qi, J. Yang, F. Liu, L. Zhang, J. Yang, X. Liu, L. Li, Y. Su, Y. Liu, R. Hao, Highly selective and robust single-atom catalyst Ru₁/NC for reductive amination of aldehydes/ketones, *Nat. Commun.* 12 (2021) 1–11.
- [11] L. Wang, M.X. Chen, Q.Q. Yan, S.L. Xu, S.Q. Chu, P. Chen, Y. Lin, H.W. Liang, A sulfur-tethering synthesis strategy toward high-loading atomically dispersed noble metal catalysts, *Sci. Adv.* 5 (2019), eaax6322.
- [12] S.K. Kaiser, Z. Chen, D. Faust Akl, S. Mitchell, J. Perez-Ramirez, Single-atom catalysts across the periodic table, *Chem. Rev.* 120 (2020) 11703–11809.
- [13] R. Qin, K. Liu, Q. Wu, N. Zheng, Surface coordination chemistry of atomically dispersed metal catalysts, *Chem. Rev.* 120 (2020) 11810–11899.
- [14] M. Babucci, A. Guntida, B.C. Gates, Atomically dispersed metals on well-defined supports including zeolites and metal-organic frameworks: structure, bonding, reactivity, and catalysis, *Chem. Rev.* 120 (2020) 11956–11985.
- [15] H. Zhuo, X. Zhang, J. Liang, Q. Yu, H. Xiao, J. Li, Theoretical understandings of graphene-based metal single-atom catalysts: stability and catalytic performance, *Chem. Rev.* 120 (2020) 12315–12341.
- [16] X. Zhang, Y. Zhou, G. Li, L. Zhang, C. Yin, Y. Yang, H. Wang, F. Feng, L. Wei, Q. Zhang, F. Yang, L. Lin, C. Lu, X. Li, A highly sulfur resistant and stable heterogeneous catalyst for liquid-phase hydrogenation, *Appl. Catal. B Environ.* 315 (2022), 121566.
- [17] Q. Yuan, Y. Gu, S. Feng, X. Song, J. Mu, B. Li, X. Li, Y. Cai, M. Jiang, L. Yan, J. Li, Z. Jiang, Y. Xu, Y. Ding, Sulfur-promoted hydrocarboxylation of olefins on heterogeneous single-Rh-site catalysts, *ACS Catal.* 12 (2022) 4203–4215.
- [18] S. Feng, X. Song, Z. Ren, Y. Ding, La-stabilized, single-atom Ir/AC catalyst for heterogeneous methanol carbonylation to methyl acetate, *Ind. Eng. Chem. Res.* 58 (2019) 4755–4763.
- [19] S. Feng, P. Hemberger, A. Bodi, X. Song, T. Yu, Z. Jiang, Y. Liu, Y. Ding, Preparation and regeneration of supported single-Ir-site catalysts by nanoparticle dispersion via nascent I radicals, *J. Catal.* 382 (2020) 347–357.
- [20] S. Feng, X. Lin, X. Song, Y. Liu, Z. Jiang, P. Hemberger, A. Bodi, Y. Ding, The role of H₂ on the stability of the single-metal-site Ir₁/AC catalyst for heterogeneous methanol carbonylation, *J. Catal.* 381 (2020) 193–203.
- [21] S. Feng, X. Lin, X. Song, B. Mei, J. Mu, J. Li, Y. Liu, Z. Jiang, Y. Ding, Constructing efficient single Rh sites on activated carbon via surface carbonyl groups for methanol carbonylation, *ACS Catal.* 11 (2020) 682–690.
- [22] Z. Ren, Y. Liu, Y. Lyu, X. Song, C. Zheng, S. Feng, J. Zhen, Y. Ding, Sing-Atom Rh based bipyridine framework porous organic polymer: a high active and superb stable catalyst for heterogeneous methanol carbonylation, *J. Catal.* 369 (2019) 249–256.
- [23] Z. Ren, Y. Liu, Y. Lyu, X. Song, Y. Liu, Dual-ionically bound single-site rhodium on porous ionic polymer rivals commercial methanol carbonylation catalysts, *Adv. Mater.* 31 (2019), 1904976.
- [24] S. Feng, X. Lin, X. Song, Y. Liu, Z. Jiang, Y. Ding, Insight into the stability of binuclear Ir–La catalysts for efficient heterogeneous methanol carbonylation, *J. Catal.* 377 (2019) 400–408.
- [25] M. Beller, *Catalytic Carbonylation Reactions*, Springer, 2006.
- [26] Y. Li, Y. Hu, X.-F. Wu, Non-noble metal-catalysed carbonylative transformations, *Chem. Soc. Rev.* 47 (2018) 172–194.
- [27] S. Feng, X. Song, Y. Liu, X. Lin, L. Yan, S. Liu, W. Dong, X. Yang, Z. Jiang, Y. Ding, In situ formation of mononuclear complexes by reaction-induced atomic dispersion of supported noble metal nanoparticles, *Nat. Commun.* 10 (2019) 1–9.
- [28] J. Zhou, Y. Zhao, C.S. Hansen, J. Yang, Y. Chang, Y. Yu, G. Cheng, Z. Chen, Z. He, S. Yu, Ultraviolet photolysis of H₂S and its implications for SH radical production in the interstellar medium, *Nat. Commun.* 11 (2020) 1–8.
- [29] H. Liu, Y. Zhou, Z. Jiang, S. Gu, X. Wei, Y. Huang, Y. Zou, H.J. Xu, QXAFS system of the BL14W1 XAFS beamline at the Shanghai synchrotron radiation facility, *Synchrotron Radiat.* 19 (2012) 969–975.
- [30] H. Funke, M. Chukalina, A.C. Scheinost, A new FEFF-based wavelet for EXAFS data analysis, *J. Synchrotron Radiat.* 14 (2007) 426–432.
- [31] P. Wisena, K.A. McGill, T. Mueller, Efficient generation of generalized Monkhorst-Pack grids through the use of informatics, *Phys. Rev. B* 93 (2016), 155109.
- [32] N.V. Ilawe, J.A. Zimmerman, B.M. Wong, Breaking badly: DFT-D2 gives sizeable errors for tensile strengths in palladium-hydride solids, *J. Chem. Theory Comput.* 11 (2015) 5426–5435.
- [33] National Institute of Standards and Technology, G. M., 20899, NIST X-ray photoelectron spectroscopy database. NIST Standard Reference Database Number 20 (2000). doi:10.18434/T4T88K ([20200610]).
- [34] B. Ledesma, J. Juárez, J. Mazarío, M. Domine, A. Beltramone, Bimetallic platinum/iridium modified mesoporous catalysts applied in the hydrogenation of HMF, *Catal. Today* 360 (2021) 147–156.
- [35] H. Jeong, G. Lee, B.-S. Kim, J. Bae, J.W. Han, H. Lee, Fully dispersed Rh ensemble catalyst to enhance low-temperature activity, *J. Am. Chem. Soc.* 140 (2018) 9558–9565.
- [36] B.C. Gates, M. Flytzani-Stephanopoulos, D.A. Dixon, A. Katz, Atomically dispersed supported metal catalysts: perspectives and suggestions for future research, *Catal. Sci. Technol.* 7 (2017) 4259–4275.
- [37] R. Qin, P. Liu, G. Fu, N. Zheng, Strategies for stabilizing atomically dispersed metal catalysts, *Small Methods* 2 (2018), 1700286.
- [38] H. Marsh, F.R. Reinoso, Activated Carbon, Elsevier, 2006.
- [39] P. Pykkö, Understanding the eighteen-electron rule, *J. Organomet. Chem.* 691 (2006) 4336–4340.
- [40] Z. Chang, W. Tang, Adsorption and reaction of methanethiol on the Ru (0 0 0 1)-p (2×2) O surface: a TPD and XPS study, *Surf. Sci.* 601 (2007) 2005–2011.
- [41] A.R.O. Ferreira, J. Silvestre-Albero, M.E. Maier, N.M.P.S. Ricardo, C. L. Cavalcante Jr, F.M.T. Luna, Sulfonated activated carbons as potential catalysts for biolubricant synthesis, *Mol. Catal.* 488 (2020), 110888.
- [42] L. Lukashuk, N. Yigit, R. Rameshan, E. Kolar, D. Teshner, M. Hävecker, A. Knop-Gericke, R. Schlögl, K. Föttinger, G.N. Rupprechter, Operating insights into CO oxidation on cobalt oxide catalysts by NAP-XPS, FTIR, and XRD, *ACS Catal.* 8 (2018) 8630–8641.
- [43] N. Feng, H. Lin, H. Song, L. Yang, D. Tang, F. Deng, J. Ye, Efficient and selective photocatalytic CH₄ conversion to CH₃OH with O₂ by controlling overoxidation on TiO₂, *Nat. Commun.* 12 (2021) 1–10.
- [44] M. Chebbi, B. Azambre, C. Volkringer, T. Loiseau, Dynamic sorption properties of metal-organic frameworks for the capture of methyl iodide, *Microporous Mesoporous Mater.* 259 (2018) 244–254.
- [45] B.M. Murphy, J. Wu, H.J. Cho, J. Soreo, C. Wang, L. Ma, B. Xu, Nature and catalytic properties of in-situ-generated brønsted acid sites on NaY, *ACS Catal.* 9 (2018) 1931–1942.
- [46] Z. Zeng, M. Altarawneh, I. Oluwoye, P. Glarborg, B.Z. Dlugogorski, Inhibition and promotion of pyrolysis by hydrogen sulfide (H₂S) and sulfanyl radical (SH), *J. Phys. Chem. A* 120 (2016) 8941–8948.
- [47] Y. Chang, Y. Yu, H. Wang, X. Hu, Q. Li, J. Yang, S. Su, Z. He, Z. Chen, L. Che, Hydroxyl super rotors from vacuum ultraviolet photodissociation of water, *Nat. Commun.* 10 (2019) 1–7.
- [48] J. Zhou, Y. Zhao, C.S. Hansen, J. Yang, Y. Chang, Y. Yu, G. Cheng, Z. Chen, Z. He, S. Yu, Ultraviolet photolysis of H₂S and its implications for SH radical production in the interstellar medium, *Nat. Commun.* 11 (2020) 1–8.
- [49] L. Gonsalvi, H. Adams, G.J. Sunley, E. Ditzel, A. Haynes, Steric and electronic effects on the reactivity of Rh and Ir complexes containing P–S, P–P, and P–O ligands. Implications for the effects of chelate ligands in catalysis, *J. Am. Chem. Soc.* 124 (2002) 13597–13612.
- [50] A. Haynes, P.M. Maitlis, G.E. Morris, G.J. Sunley, H. Adams, P.W. Badger, C. M. Bowers, D.B. Cook, P.I.P. Elliott, T. Ghaffar, H. Green, T.R. Griffin, M. Payne, J. M. Pearson, M.J. Taylor, P.W. Vickers, R.J. Watt, Promotion of iridium-catalyzed methanol carbonylation: Mechanistic studies of the creative process, *J. Am. Chem. Soc.* 126 (2004) 2847–2861.
- [51] A. Haynes, *Catalytic Methanol Carbonylation*, 53, Elsevier, 2010, pp. 1–45.
- [52] Z. Ren, Y. Lyu, X. Song, Y. Ding, Review of heterogeneous methanol carbonylation to acetyl species, *Appl. Catal. A Gen.* 595 (2020), 117488.
- [53] P. Kalck, C. Le Berre, P. Serp, Recent advances in the methanol carbonylation reaction into acetic acid, *Coord. Chem. Rev.* 402 (2020), 213078.